The catalytic mechanism of electron-bifurcating electron transfer flavoproteins (ETFs) involves an intermediary complex with NAD$^+$

Gerrit J. Schut[‡], Nishya Mohamed-Raseek[§], Monika Tokmina-Lukaszewska[¶], David W. Mulder[||], Diep M. N. Nguyen[‡], Gina L. Lipscomb[‡], John P. Hoben[§], Angela Patterson[¶], Carolyn E. Lubner[||], ⓘ Paul W. King[||], John W. Peters[**], Brian Bothner[¶], ⓘ Anne-Frances Miller[§], and ⓘ Michael W. W. Adams[‡1]

From the [‡]Department of Biochemistry and Molecular Biology, University of Georgia, Athens, Georgia 30602-7229, the [§]Department of Chemistry, University of Kentucky, Lexington, Kentucky 40506, the [¶]Department of Chemistry and Biochemistry, Montana State University, Bozeman, Montana 59717, the [||]Biosciences Center, National Renewable Energy Laboratory, Golden, Colorado 80401, and the [**]Institute of Biological Chemistry, Washington State University, Pullman, Washington 99164

Edited by Ruma Banerjee

Electron bifurcation plays a key role in anaerobic energy metabolism, but it is a relatively new discovery, and only limited mechanistic information is available on the diverse enzymes that employ it. Herein, we focused on the bifurcating electron transfer flavoprotein (ETF) from the hyperthermophilic archaeon *Pyrobaculum aerophilum*. The EtfABCX enzyme complex couples NADH oxidation to the endergonic reduction of ferredoxin and exergonic reduction of menaquinone. We developed a model for the enzyme structure by using nondenaturing MS, cross-linking, and homology modeling in which EtfA, -B, and -C each contained FAD, whereas EtfX contained two [4Fe-4S] clusters. On the basis of analyses using transient absorption, EPR, and optical titrations with NADH or inorganic reductants with and without NAD$^+$, we propose a catalytic cycle involving formation of an intermediary NAD$^+$-bound complex. A charge transfer signal revealed an intriguing interplay of flavin semiquinones and a protein conformational change that gated electron transfer between the low- and high-potential pathways. We found that despite a common bifurcating flavin site, the proposed EtfABCX catalytic cycle is distinct from that of the genetically unrelated bifurcating NADH-dependent ferredoxin NADP$^+$ oxidoreductase (NfnI). The two enzymes particularly differed

in the role of NAD$^+$, the resting and bifurcating-ready states of the enzymes, how electron flow is gated, and the two two-electron cycles constituting the overall four-electron reaction. We conclude that *P. aerophilum* EtfABCX provides a model catalytic mechanism that builds on and extends previous studies of related bifurcating ETFs and can be applied to the large bifurcating ETF family.

Electron-bifurcating enzymes couple exergonic and endergonic reactions, thus maximizing conservation of free energy available from exergonic reactions (1). In this way, electrochemical energy can be captured for cellular metabolism, lowering the demands on transmembrane gradients or substrate-level phosphorylation. Thus, electron bifurcation provides a unifying explanation for many peculiar fermentative pathways found in anaerobic microorganisms, with important implications for understanding anaerobic microbial physiology in general (2–9).

So far, the bifurcating enzymes that have been characterized fall into one of four phylogenetically unrelated groups: electron transfer flavoproteins (EtfAB-containing), [FeFe]-hydrogenase/formate dehydrogenases (HydABC-containing), heterodisulfide reductases (HdrA-containing), and transhydrogenases (NfnAB-containing) (8, 10). These enzymes catalyze more than a dozen different reactions, most involving the oxidation or reduction of ferredoxin, and are found mainly in anaerobic organisms (reviewed in Refs. 3, 8, 11, and 12). However, some of the EtfAB-containing complexes, such as that described below, can also be found in microaerophiles and aerobes.

Bifurcating ETFs[2] are the best-studied bifurcating enzymes, and they form a subset of the large and well-known family of ETFs, which are found in all domains of life (13–15). Whereas the nonbifurcating ETFs contain one FAD and one AMP per AB heterodimer, the bifurcating EtfABs contain two FAD mol-

[2] The abbreviations used are: ETF, electron transfer flavoprotein; BF-FAD, bifurcating flavin; ET-FAD, electron transfer flavin; QR-FAD, quinone reductase flavin; Fd, ferredoxin; BS3, bis(sulfosuccinimidyl)suberate; GEE, glycine ethyl ester; DnsCl, dansyl chloride; MQ, menaquinone; ASQ, anionic semiquinone; TAS, transient absorption spectroscopy; CT, charge transfer; NSQ, neutral semiquinone; Bistris propane, 1,3-bis[tris(hydroxymethyl)methylamino]propane.

🇫ASBMB
Published in the U.S.A.

J. Biol. Chem. (2019) 294(9) 3271–3283 **3271**

ecules, with the additional FAD replacing the AMP of the canonical ETF (13, 16, 17). The functions of bifurcating ETFs have been established in several strictly anaerobic micoorganisms. For example, the butyryl-CoA dehydrogenase (EtfAB–Bcd) complex from the butyrate-producing *Acidaminococcus fermentans* accomplishes the endergonic reduction of ferredoxin (Fd) with NADH by driving it with the exergonic reduction of crotonyl-CoA by NADH (16). Likewise, the strict anaerobe *Acetobacterium woodii* can utilize lactate as a carbon source using the bifurcating LDH–EtfAB complex to drive the endergonic oxidation of lactate to pyruvate with the energy provided by the exergonic electron transfer from reduced Fd to NAD$^+$ (18). *A. woodii* can also utilize caffeate as an electron acceptor in which EtfAB-containing caffeyl-CoA reductase complex (CarCDE) couples the exergonic reduction of caffeyl-CoA by NADH to the endergonic reduction of Fd by NADH (19). *Megasphaera elsdenii* similarly contains a lactate dehydrogenase and a Bcd that likely interact with the same EtfAB (20–22).

Bifurcating ETFs are also found in some microorganisms that are capable of fixing atmospheric nitrogen, such as the aerobe *Azotobacter vinelandii* (13, 23, 24). In *A. vinelandii*, an enzyme complex containing EtfAB and quinone reductase, termed FixABCX, is associated with nitrogen-fixing activity (13, 24). The FixAB subunits are referred to as bifurcating Etf, whereas the FixCX subunits are referred to as Etf-quinone oxidoreductase (13). FixABCX is thought to provide reduced Fd for nitrogen fixation through the quinone-dependent reduction of Fd with NADH (23, 24). However, genomic analyses reveal that FixABCX-like complexes are not restricted to diazotrophs, indicating a general role extending beyond nitrogen fixation (13). We will refer to such complexes as EtfABCX to recognize their homology with FixABCX while also alluding to broader metabolic roles.

Herein we describe the mechanism for the first EtfABCX to be characterized from a non-nitrogen-fixing respiratory microorganism. Our exemplar was obtained from *Pyrobaculum aerophilum*, a denitrifying microaerophilic crenarchaeote that grows at 100 °C. *P. aerophilum* oxidizes organic compounds using oxygen, nitrate, arsenate, selenate, iron, and thiosulfate as terminal electron acceptors (25), but its genome lacks the genes for nitrogen fixation (26). The genes encoding *P. aerophilum* EtfABCX were expressed in the fermentative hyperthermophile, *Pyrococcus furiosus*, and both EtfABCX and the EtfAB subcomplex were purified. Like the Fix system (24), *P. aerophilum* EtfABCX is shown to oxidize NADH and bifurcate electrons to both high-potential (quinone) and low-potential (Fd) acceptors. For the *P. aerophilum* EtfABCX complex, we refer to each of the flavins in the enzyme in terms of the role that each has been proposed to play in ETF proteins in general (13, 16, 24, 27). Thus, the FAD unique to bifurcating ETFs is denoted the "bifurcating FAD," or BF-FAD, and this is present in the A-subunit of *P. aerophilum* EtfABCX (Fig. 1). The electron-transferring FAD or ET-FAD is the FAD that is shared with the structurally homologous nonbifurcating ETFs that appear to specialize in electron transfer between partner proteins (13, 14, 28). By homology, the ET-FAD in *P. aerophilum* EtfABCX is located in the B subunit, whereas the FAD in the C subunit is referred to as the QR-FAD, as it is likely the site of quinone reduction (Fig. 1).
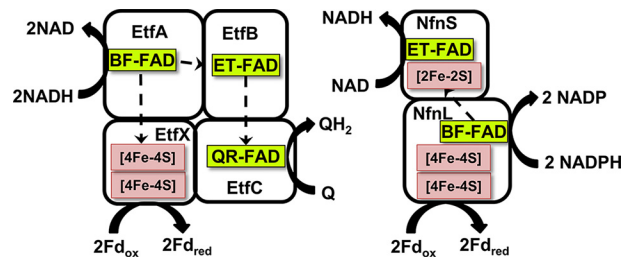
Figure 1. Cofactor content and proposed pathway of electron flow in *P. aerophilum* EtfABCX and *P. furiosus* NfnI. *Q*, quinone; *QH$_2$*, reduced quinone; *Fd$_{ox}$*, oxidized ferredoxin; *Fd$_{red}$*, reduced ferredoxin.

The primary goal of this work was to elucidate the overall catalytic cycle of *P. aerophilum* EtfABCX. Structural studies of related ETF complexes have shown that large conformational changes occur during catalysis, and a mechanism involving relatively large domain movement has been proposed (16, 29, 30). However, more information is needed to understand how electron flow to the high- and low-potential acceptors is gated and controlled. It was also important to determine how the catalytic cycle of EtfABCX compared with that recently established for the bifurcating enzyme, NADH-dependent ferredoxin NADP oxidoreductase I (NfnI) from *P. furiosus* (31). NfnI and EtfABCX have very similar cofactor compositions, even though they are completely unrelated phylogenetically, and both use NAD(P)H as the mid-potential donor to their BF-FADs and use Fd as the low-potential carrier that is reduced or oxidized by a pair of [4Fe-4S] clusters (Fig. 1). However, herein we have identified key catalytic intermediates of *P. aerophilum* EtfABCX, including a novel NAD$^+$-dependent charge transfer complex, and describe a catalytic cycle that is very distinct from that established for NfnI. Moreover, the *P. aerophilum* EtfABCX catalytic cycle is consistent with previous structural observations and mechanisms of related EtfAB-containing complexes (8, 9, 13, 24, 27). We propose that the unifying principles proposed here can be applied to all bifurcating members of the large ETF family.

Results

Structure and catalytic activity of EtfAB and EtfABCX

The His-tagged form of *P. aerophilum* EtfABCX was produced in *P. furiosus.* Size-exclusion chromatography of the purified enzyme resolved two peaks that corresponded (by MS analysis) to EtfABCX, eluting near 450 kDa, and EtfAB, eluting near 50 kDa. The former is consistent with a tetrameric form of the EtfABCX complex (with a calculated mass of 125 kDa for the heterotetramer), whereas the latter peak corresponds to the EtfAB heterodimer (with a calculated mass of 66 kDa). Although EtfABCX is thought to interact with the cell membrane *in vivo* and to reduce quinone, the enzyme was purified from the cytoplasmic fraction of *P. furiosus*, is stable in solution, and, in contrast to the FixABCX system (24), does not require detergent to maintain solubility. Analyses of *P. aerophilum* EtfAB by native MS gave the expected mass with two FAD bound (measured: 69,562.45 Da; calculated: 69,566.17 Da; Fig. S1). The A and B subunits were not separated by the collision energy during MS analysis, by reverse phase LC under acidic conditions, or by the presence of an organic solvent, implying

great stability for the heterodimer. The EtfC subunit was also identified by MS with a mass consistent with a bound FAD cofactor (Fig. S2). Based on MS analysis conducted under native and denaturing conditions, we conclude that as purified, both EtfAB and the EtfABCX holoenzyme have full flavin occupancy.

To predict the most probable three-dimensional structure of individual subunits, the protein fold recognition tool Phyre2 was used (32). To determine the tertiary structure of the protein of interest, this relies on sequence alignment, secondary structure prediction, and finally the match of predicted folds to homologous proteins with known protein structure. In the next step, the energy-minimized homology models of *P. aerophilum* Etf were overlaid on the structure of the recently published model of FixABCX from *Azotobacter vinelandii* (24). Once the quaternary structure was in place, cofactor-binding sites were modeled using individually refined models of *P. aerophilum* EtfAB, -C, or -X, generated based on templates 1O97.pdb (EtfAB domain II), 4L2I.pdb (EtfAB, domains I and III), 2GMH.pdb (EtfC), and 2PVZ.pdb (EtfX) in Swiss Modeler, followed by manual adjustment of a few side chains and unstructured strands and then energy minimization.

To validate the structural model of the complete *P. aerophilum* EtfABCX complex, three complementary experimental approaches were employed: 1) noncovalent MS to establish the mass of the entire complex in its native form, confirm the presence of cofactors, and determine cofactor and protein component stoichiometry; 2) chemical cross-linking and peptide-based MS to ascertain protein–protein interaction networks and distance constraints; and 3) surface labeling coupled to MS to map the solvent-exposed surfaces. Iterative modeling was then used, in which data from approaches 1−3 were used to test a model, identify inconsistencies, adapt the model, and repeat (24, 33–39). To preserve noncovalent interactions at protein interfaces, the homobifunctional cross-linking reagent, bis(sulfosuccinimidyl)suberate (BS3) was used. BS3 can probe a wide distribution of distances and bridge spatially close primary amine– and hydroxyl– containing amino acid residues (40). To probe the solvent-accessible surface of the intact complex and to obtain the most complementary results, two surface-labeling reagents, glycine ethyl ester (GEE) and dansyl chloride (DnsCl), were used. GEE and DnsCl target carboxyl, primary amine, and hydroxyl groups, which collectively are the most prevalent groups on protein surfaces, allowing for a detailed mapping of solvent-exposed residues. The model shown in Fig. 2 was in agreement with 37% of identified connections, including inter- and intrasubunit cross-links. Taking into account the distance a cross-linker can cover and the conformations a residue can adopt in solution, it is considered a good result if 30% of all generated cross-links within the complex are satisfied (33). Our best model was also in agreement with about 87% of the surface labels. The complete information on the generated cross-links and surface labels satisfying the *P. aerophilum* EtfABCX complex model can be found in Table S1 and Fig. S3, respectively.

The EtfABCX model shows that one of the [4Fe-4S] clusters in EtfX is within 10 Å of the BF-FAD, which should support rapid direct electron transfer. Although the BF- and ET-FAD are 16 Å apart and the distance between the isoalloxazine rings
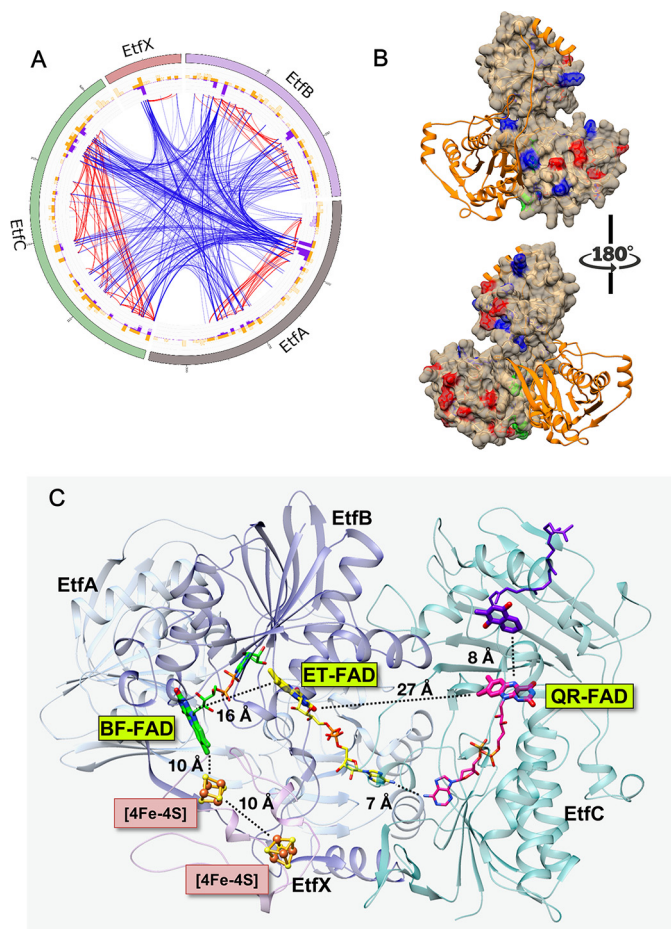

Figure 2. *A*, the *multilayer circular plot* presents interactions within the *P. aerophilum* EtfABCX complex captured by cross-linking (BS3). The most outer layer represents the protein sequence: EtfA is shown in *gray*, EtfB is *purple*, EtfC is *green*, and EtfX is *pink*. *Yellow* and *purple histograms* show the location of BS3 target residues (Lys and Ser) and the density of cross-links, respectively. *Blue lines* represent connections between subunits (intersubunit cross-links), and *red lines* highlight interactions within a single unit (intrasubunit cross-links). Cross-links maintaining less than 20 ppm error and a score higher than 3 (a score >2 is considered significant) are displayed. *B*, protein surface map of the complete *P. aerophilum* EtfABCX complex (for simplicity, only the AB dimer is presented) shows GEE (modification sites shown in *red*) and DnsCl (modification sites shown in *blue*) labels incorporated in to the native complex during short exposure to the two labeling reagents. Residues at the dimer interface highlighted in *green* correspond to labels integrated into the structure exclusively in the latest time points. Individual proteins are *color-coded* as follows: EtfB in *orange* and EtfA in *tan*. *C*, ribbon diagram of the MS-validated EtfABCX model. EtfA and EtfB are shown in *light* and *dark blue*, respectively, EtfC is *teal*, EtfX is *magenta*, the BF-FAD is *green*, the ET-FAD is *yellow*, and the QR-FAD is *pink*. Organic cofactors are shown using *thick sticks* to emphasize the redox-active portions and *thin sticks* to complete the structures. Iron–sulfur clusters are shown in *orange* (*Fe*) and *yellow* (*S*), and the menaquinone (*purple*) was modeled using the 2GMH (porcine electron transfer flavoprotein-ubiquinone oxidoreductase) structure with bound ubiquinone.

of the ET- and the QR-flavins is almost 30 Å, similar distances have been reported for the analogous flavins in the bifurcating EtfAB–Bcd and CarCDE complexes (29, 30). Both of these complexes undergo a large conformational change as part of the catalytic cycle, and such changes are also incorporated as part of the mechanism of *P. aerophilum* EtfABCX proposed herein.

P. aerophilum EtfABCX is thought to couple the reversible oxidation of NADH to the reduction of Fd and menaquinone (MQ), by analogy with FixABCX, according to Reaction 1.

$$2NADH + 2Fd_{OX} + MQ \rightarrow 2NAD^+ + 2Fd_{red} + MQH_2$$
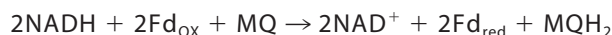
<div align="center">Reaction 1</div>

The primary Fd in *P. aerophilum* contains a single [4Fe-4S] cluster (41) and transfers a single electron (Reaction 1), whereas MQ is thought to be the natural quinone component of the *P. aerophilum* respiratory system (42). The purified forms of both EtfAB and EtfABCX catalyzed the oxidation of NADH and reduced the artificial electron carrier iodonitrotetrazolium with specific activities of 41.8 ± 6.5 and 15.8 ± 2.7 μmol of NADH oxidized/min/mg (at 80 °C), respectively. Although EtfC is proposed to reduce MQ *in vivo*, both EtfAB and EtfABCX also oxidized NADH and reduced the water-soluble MQ analog, menadione. The specific activities were 8.8 ± 0.8 and 5.1 ± 1.2 μmol of NADH oxidized/min/mg (at 80 °C), respectively. The lack of specificity with respect to the quinone acceptor makes it difficult to directly measure the bifurcation activity of EtfABCX, which is further complicated by the fact that menadione and NADH have similar absorption spectra (24). Bifurcation activity of EtfABCX was therefore assessed by coupling the oxidation of reduced menadione and reduced Fd to the reduction of NAD^+, which was followed by the fluorescence of the NADH that was generated. The Fd used in this reaction was that of *P. furiosus*, which also contains a single [4Fe-4S] cluster (43). Importantly, reduction of NAD^+ by EtfABCX depended upon the presence of both reduced Fd and reduced menadione, and no bifurcation activity was detected using EtfAB (Fig. S4). With the FixABCX from N_2-fixing *A. vinelandii*, a 25% increase in activity was observed when all substrates (NADH, quinone, and Fd) were present relative to when only NADH and quinone were present (24), whereas in the case of *P. aerophilum* EtfABCX, an ~2-fold increase was observed (Fig. S4).

The reduction potentials of the flavins in EtfAB

The optical signatures of the two flavins of EtfAB were monitored over the course of stepwise reduction with sodium dithionite or titanium citrate in the absence of mediators (Figs. S5*A* and S6). The initial increase in absorbance at 374 nm, where the anionic semiquinone (ASQ) of flavin absorbs maximally, was accompanied by a decrease at 454 nm (absorption maximum of oxidized flavin), indicating that an FAD undergoes a 1 e⁻ reduction to ASQ (Fig. S5, phase 1). We assigned this to the ET-FAD, as it is expected to be more readily reduced than the BF-FAD (17, 27). Further addition of reductant resulted in only a slight intensity loss at 374 nm, suggesting little change in the amount of ASQ (Fig. S5, phase 2, staggered or nested mechanisms). As discussed further below, to account for these observations, we propose that a radical is present on either the ET-FAD or the BF-FAD, leading to the observed optical signal. This ASQ signal also persisted upon the addition of excess titanium citrate (this was also true with excess dithionite, although less clear; see Figs. S5*A* and S6).

Titrations in the presence of redox mediators showed that one flavin undergoes reduction from OX to ASQ to HQ before the other is reduced from OX to HQ (Fig. S5*C*, sequential). Thus, in Fig. S7*A*, the initial negative difference absorbance
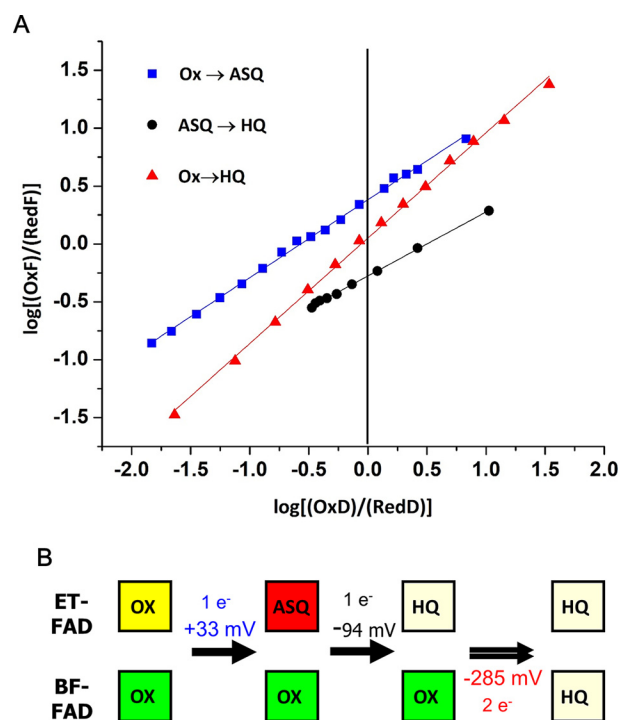
Figure 3. *A*, slopes of Nernst plots confirm the 1 e⁻ nature of events in phases 1 and 2 and the 2 e⁻ nature of phase 3. Best linear fits are as follows: phase 1 (*blue*), $0.66x + 0.55$ ($R^2 = 0.997$); phase 2 (*black*), $0.55x - 0.27$ ($R^2 = 0.999$), and phase 3 (*red*), $0.91x + 0.05$ ($R^2 = 0.998$). For the data in *blue* the "oxidized" flavin is *OX*, "reduced" flavin is the *ASQ*, and the dye is thionine. For the data in *black* the oxidized flavin is *ASQ*, reduced flavin is the *HQ*, and the dye is Nile blue. For the data in *red*, oxidized flavin is *OX*, reduced flavin is *HQ*, and the dye is safranin-O. *B*, proposed reduction events for each FAD cofactor in EtfAB and the measured potentials.

near 374 nm clearly indicates that ASQ is formed, whereas the positive intensity at 454 nm represents the OX signature lost in the course of this reaction (OX at the beginning exceeds OX at the end; Fig. S5*A*). Conversion of the ET-FAD from OX to ASQ occurred with an E_m of 33 ± 6 mV (Fig. 3). The slope of the line near 0.5 confirms that the reaction in question is a 1 e⁻ reaction and therefore rules out reduction to HQ. Difference spectra associated with phase 2 of the reductive titration (Fig. S5*B*) indicate that it corresponds to net reduction of an ASQ to HQ (Fig. S7*B*). These data clearly show net loss of the ASQ features. The slope of the Nernst log/log plot in Fig. 3 confirms this event as a 1 e⁻ reaction. The intercept of the Nernst log/log plot yields an E_m value for ET-FAD (ASQ/HQ) of -94 ± 7 mV. Titration of the lower-potential FAD (Fig. S7*C*, phase 3) reveals no significant contribution from ASQ, and the slope of 1 of the Nernst log/log plot confirms that this phase corresponds to a 2 e⁻ reduction (Fig. 3*A*). An E_m value for BF-FAD (OX/HQ) of -285 ± 5 mV was determined, which is close to the value of -279 mV reported for the bifurcating EtfAB from *M. elsdenii* (21). Thus, we conclude that the higher-potential FAD, ET-FAD, is reduced via two sequential 1 e⁻ events to HQ but that the lower potential FAD, BF-FAD, undergoes reduction directly to the HQ state in a 2 e⁻ event under equilibrium conditions (Fig. 3*B*). The values measured for *P. aerophilum* EtfAB of $E_{m(OX/ASQ)} = +33$ mV and $E_{m(ASQ/HQ)} = -94$ mV fall well within values reported for other EtfABs (21, 27), and the high $E_{m(OX/ASQ)}$ of $+33$ mV for *P. aerophilum* EtfAB indicates that

the resting state of the EtfAB dimer possesses ET-FAD in its ASQ state.

Transient absorption spectroscopy of EtfAB and EtfABCX

The SQ state of the BF-FAD was not observed in steady-state titrations, so transient absorption spectroscopy (TAS) was used to probe for short-lived flavin species. Formation of an ASQ with loss of absorption from the oxidized flavin was observed for both EtfAB and EtfABCX (Fig. S8). In each, the ASQ kinetic trace was best fit with two components corresponding to lifetimes of 60 and 1080 ps, suggesting that they arise from distinct flavins that are present in both EtfAB and EtfABCX. We therefore assigned the 60- and 1080-ps SQ components to the BF- and ET-FAD, respectively, based on the titration results that show the BF-FAD generates a more thermodynamically unstable ASQ than ET-FAD. In addition to the ASQ signal, we also observed the presence of a signal at ~570 nm, suggesting that there is emission from FAD OX, the origin of which is unknown (Fig. S8*A*). The formation of flavin SQ states was further studied by visible and EPR spectroscopy, as discussed below.

Reductive titrations of EtfAB

The spectral features around 374 nm of as-purified EtfAB were assigned to an ASQ, and this was converted to the fully oxidized form by exposure to air (Fig. 4*A* and Fig. S6). Stepwise reduction of air-oxidized EtfAB with NADH regenerated the ASQ seen in the as-purified complex (prior to air oxidation), as indicated by spectral features at 374 nm with a shoulder at 398 nm. These reached a maximum with the addition of about half an equivalent of NADH (Fig. 4*A* and Fig. S9). To explain how a two-electron hydride transfer from NADH generates a singly reduced ASQ state on the ET-FAD, we propose intermolecular electron transfer between two EtfAB molecules, as was suggested for the NADH-induced ASQ state of the related EtfAB–Bcd complex of *A. fermentans* (16, 29). These data with *P. aerophilum* EtfAB therefore confirm the conclusion from the equilibrium titrations that the ET-FAD rests in the ASQ state when the complex is "ready" for bifurcation. EtfAB appeared fully reduced upon further addition of NADH to more than 2 eq, as shown by the lack of absorption at 454 nm. In addition, a strong charge transfer (CT) band feature is seen from 550 to 1000 nm (Fig. 4*A* and Fig. S9). The reduction of *A. fermentans* EtfAB with NADH showed a similar absorption spectrum, although the CT band was not as obvious (16). The CT band has to arise from the interaction of NAD^+ with the BF-FAD because the ET-FAD does not interact with NAD(H) (13). Considering that NADH adds two electrons to the EtfAB core, there must be a flavin radical present (with three electrons distributed between two FAD cofactors); however, this is not obvious from the UV-visible spectrum.

EPR spectroscopy was used to directly probe for the presence and nature of radical species (44, 45). *P. aerophilum* EtfAB, as purified anaerobically in the absence of reductants, displayed a weak radical centered at g = 2.006 (0.1 spin mol^{-1}), and this increased slightly (to 0.2 spin mol^{-1}) upon the addition of NADH (Fig. 5). In contrast, reduction of EtfAB with excess sodium dithionite produced an intense anisotropic radical sig-
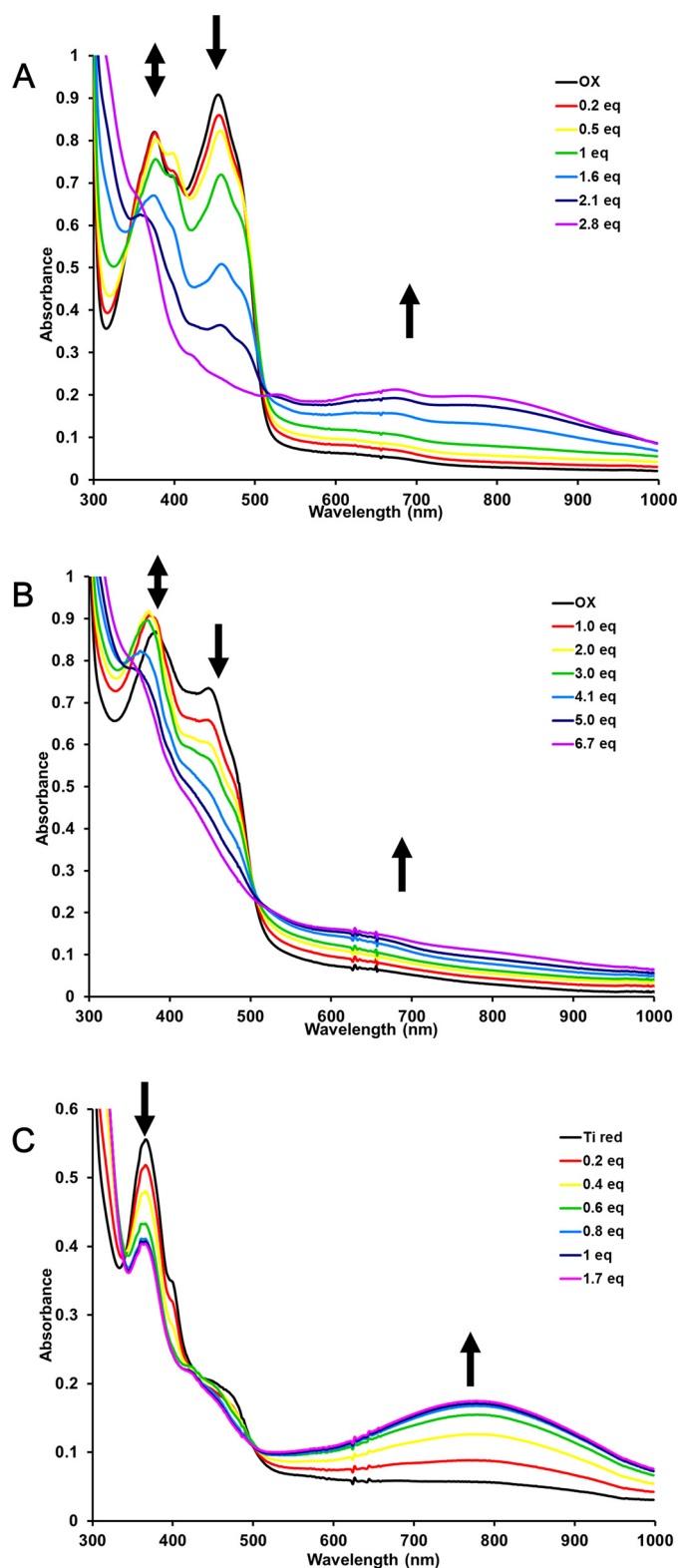
Figure 4. Titration of *P. aerophilum* EtfAB (74 μM) (*A*) and EtfABCX (15 μM) (*B*) with NADH. *Arrows* (*left* to *right*) indicate formation and disappearance of the ASQ, disappearance of OX flavin absorbance, and the formation of a broad CT complex. *C*, anaerobic titration with NAD^+ of *P. aerophilum* EtfAB (74 μM) reduced with excess titanium citrate. *Arrows* (*left* to *right*) indicate the disappearance of ASQ and the formation of a broad CT complex.
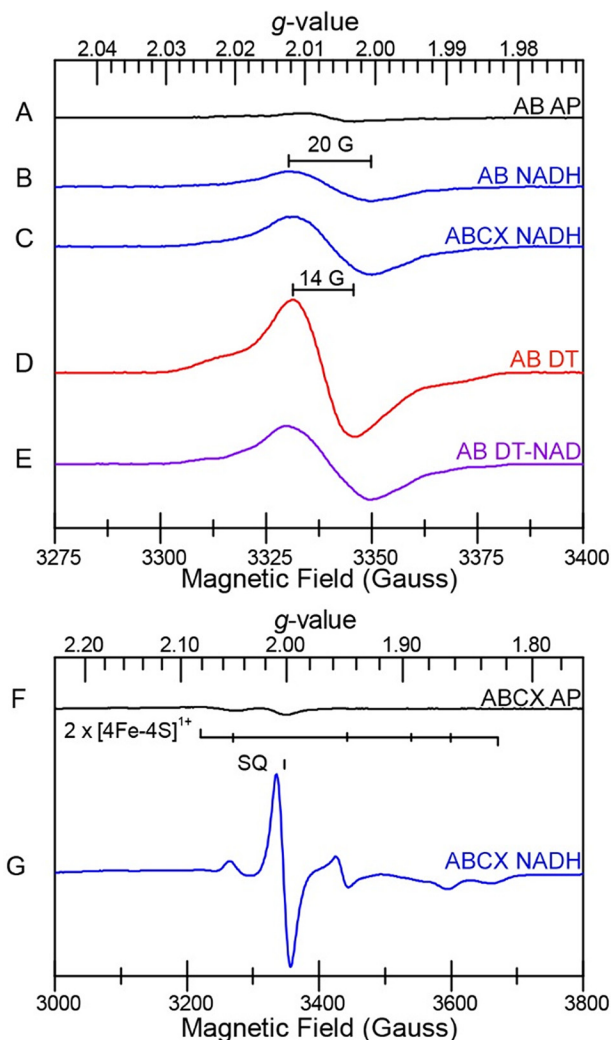
Figure 5. EPR spectra (9.38 GHz CW) of *P. aerophilum* EtfAB and EtfABCX. The samples are as follows. *AB AP*, as-purified EtfAB; *AB NADH*, EtfAB treated with NADH; *ABCX NADH*, EtfABCX treated with NADH; *AB DT*, EtfAB treated with sodium dithionite; *AB DT-NAD*, EtfAB sequentially treated with sodium dithionite and NAD⁺; *ABCX AP*, EtfABCX as purified; *ABCX NADH*, EtfABCX treated with NADH. *Top spectra* (*A–E*) were recorded at 77 K, and *bottom spectra* (*F* and *G*) were recorded at 10 K.

nal centered at g = 2.007 representing ∼1.0 spin mol⁻¹. The narrow line width (14 G) is indicative of an ASQ radical (46), in agreement with the absorption data (see below) indicating that an ASQ radical is the source of this signal; however, it is not clear whether the radical resides on the BF- or ET-FAD. The addition of NAD⁺ to the dithionite-reduced sample decreased the EPR absorption by 50% and broadened the line width of the radical signal (from 14 to 20 G). Although change in line width is suggestive of a neutral semiquinone (NSQ) flavin radical (45), this broadening of the radical signal more likely reflects interactions of the BF-FAD with NAD⁺ affecting the optical and paramagnetic signal of the ASQ radical.

Similarly, treatment of *P. aerophilum* EtfAB with the chemical reductant titanium citrate (Fig. S6) generated an ASQ state that persisted even in the presence of excess reductant (Fig. 4C). We propose that this corresponds to the 3 e⁻ reduced state of EtfAB. However, upon the addition of NAD⁺ to titanium-reduced EtfAB, the optical ASQ signa-

ture is lost, and a CT complex is generated (Fig. 4C and Fig. S10). It should be noted that this CT signature is slightly different (less absorbance in the 680-nm region) from that observed after treatment of EtfAB with excess NADH, where NAD⁺ is generated *in situ* (compare Figs. S9 and S10). These data confirm that NAD⁺ binding to the BF-FAD site changes the electronic state of the EtfAB core, whereby the usual absorption spectrum of the ASQ is not observed even though a radical can be seen by EPR analysis (Fig. 5). Thus, it appears that a 3 e⁻ reduced state of EtfAB accumulates upon reduction with NADH and by chemical reductant, based on both optical and EPR spectroscopy.

Reductive titrations of EtfABCX

The response of EtfABCX to chemical reductants and to NAD(H) was similar to that of EtfAB (Fig. 4 and Figs. S11 and S12) but more complex due to the additional flavin (QR-FAD) in EtfC and the two [4Fe-4S] clusters in EtfX. Titration of EtfABCX with NADH forms an intermediate ASQ that disappears and is replaced by absorption from an NSQ near 620 nm, mixed with the broad absorption of the CT complex, which we assigned to the interaction of NAD⁺ with the EtfAB core (Fig. S12). The additional flavin radical (the NSQ) we assigned to the QR-FAD in EtfC. A strong semiquinone radical signal (0.5 spins mol⁻¹) at g = 2 was observed upon reduction of EtfABCX with excess NADH, in addition to several overlapping broad signals spanning the g = 2.08 –1.80 region indicative of reduced iron–sulfur clusters (Fig. 5). The semiquinone EPR signal centered at g = 2.006 was resolved at 77 K. The line width (20 G) is most consistent with it originating from an NSQ radical (45) (Fig. 5C), possibly from the QR-FAD in EtfC (Fig. 1). The broad EPR signals were most intense near 10 K and disappeared above 30 K (Fig. 5G), consistent with the relaxation properties of reduced [4Fe-4S]¹⁺ clusters. The reduction potentials of the two [4Fe-4S] clusters in *P. furiosus* Nfn (see Fig. S13) were estimated at −513 and −718 mV by direct electrochemistry (31), but unfortunately, *P. aerophilum* EtfABCX was not responsive to this approach.

The reduction by NADH of the lower-potential [4Fe-4S] clusters of EtfX is further evidence of the bifurcating activity of *P. aerophilum* EtfABCX, as is formation of the QR-FAD of EtfC to generate an NSQ seen by visible absorption. In addition, NAD⁺ also interacts with chemically reduced *P. aerophilum* EtfABCX, yielding CT bands, but, as with EtfAB, the spectrum is slightly different (lacking some of the 680-nm features) from that induced by NADH treatment alone, indicating that the CT bands are an inherent property of the interaction of NAD⁺ with the EtfAB core.

Discussion

The data presented herein show that the *P. aerophilum* EtfAB core possesses several crucial prerequisites for bifurcating activity: 1) a bifurcating flavin that accepts electron pairs from NADH, 2) a high potential electron transfer pathway consisting of a high-potential flavin (E_m = −94 mV for the ASQ/HQ couple of ET-FAD) linking the bifurcating flavin to the quinone pool via QR-FAD, and 3) a low potential pathway by which the BF-FAD reduces Fd (via the two 4Fe clusters in

EtfX). Our measured E_m (-285 mV) for the OX/HQ couple of BF-FAD is more positive than that of NADH ($E^{0'}$ -320 mV), indicating favorable electron transfer but with minimal dissipation of energy. However, the BF-FAD does not display a stable SQ state in our mediated equilibrium titrations, which suggests that it exhibits crossed potentials where its E_m ASQ/HQ is more positive than its E_m OX/ASQ, although their average must correspond to the measured E_m OX/HQ of -285 mV (ASQ is proposed based on its observation by TAS). Thus, we can calculate a lower limit for the E_m of the BF-FAD ASQ/HQ couple. Assuming that the ASQ/HQ couple of the ET-FAD is operative in turnover (27, 30), electron transfer to ASQ-ET-FAD at -94 mV is exergonic by 191 mV. It follows that electron transfer to Fd can be endergonic at a similar level, placing a lower boundary of -476 mV on the E_m of the BF-FAD OX/ASQ, which is presumably sufficient to reduce Fd (3, 47). For the respiratory bifurcating bc_1 complex, a stability constant for the low potential SQ state of the bifurcating quinone was estimated at ~10^{-15}, from which a potential span of ~900 mV between the first high-potential electron and the second low-potential electron was derived (48). This concept has been adapted to calculate the potentials of other bifurcating centers, including several EtfAB-containing complexes (reviewed in Ref. 8). Although the quinone value does not apply to a flavin system, which has very different chemistry, it puts our value in perspective. When it is applied to *P. aerophilum* EtfABCX, we calculate a ASQ/HQ couple of $+165$ mV ($-285 + (900 \text{ mV}/2)$) and an OX/ASQ couple of -735 mV ($-285 - (900 \text{ mV}/2)$). Hence, based on these two approaches, we estimate the E_m of ASQ/HQ to be between -94 and $+165$ mV and that of OX/ASQ to be between -735 and -476 mV, with an average corresponding to the measured value of -285 mV. These values are well within the range proposed previously for other Etf-type complexes and are consistent with the thermodynamically favorable reduction of Fd with an E_m of approximately -500 mV (8, 30, 48).

As shown in Fig. 6, we propose that, based on the equilibrium titration data, the 1 e⁻ reduced state of EtfAB within the EtfABCX complex is the resting form of the enzyme. This accepts a hydride from NADH to generate the HQ-BF-FAD in close proximity to ASQ-ET-FAD, in which the NAD⁺ stays bound and forms a NAD⁺·BF-FAD$_{HQ}$ CT complex. The BF- and ET-FAD could share an electron switching between HQ-BF-FAD/ASQ-ET-FAD and ASQ-BF-FAD/HQ-ET-FAD, and the stable CT complex is formed by the strong interaction of NAD⁺ with BF-FAD, as shown in Fig. 6. In this state, the EtfAB subcomplex is "hot" and can transfer the low-potential electron from the BF-FAD to Fd through the proximal and distal iron–sulfur clusters in EtfX, leaving the EtfAB subcomplex as OX-BF-FAD/HQ-ET-FAD. The distance between the ET-FAD and the QR-FAD is too far for efficient electron transfer (Fig. 2 and Refs. 16, 21, 29, 30, and 49), but it has been proposed that ETF-type complexes undergo a large conformational change as part of the catalytic cycle (16, 21, 29, 30). We suggest that this is triggered by oxidation of the ASQ-BF-FAD and brings the ET-FAD close enough to the QR-FAD for electron transfer into the high-potential active site (30). The high-potential elec-
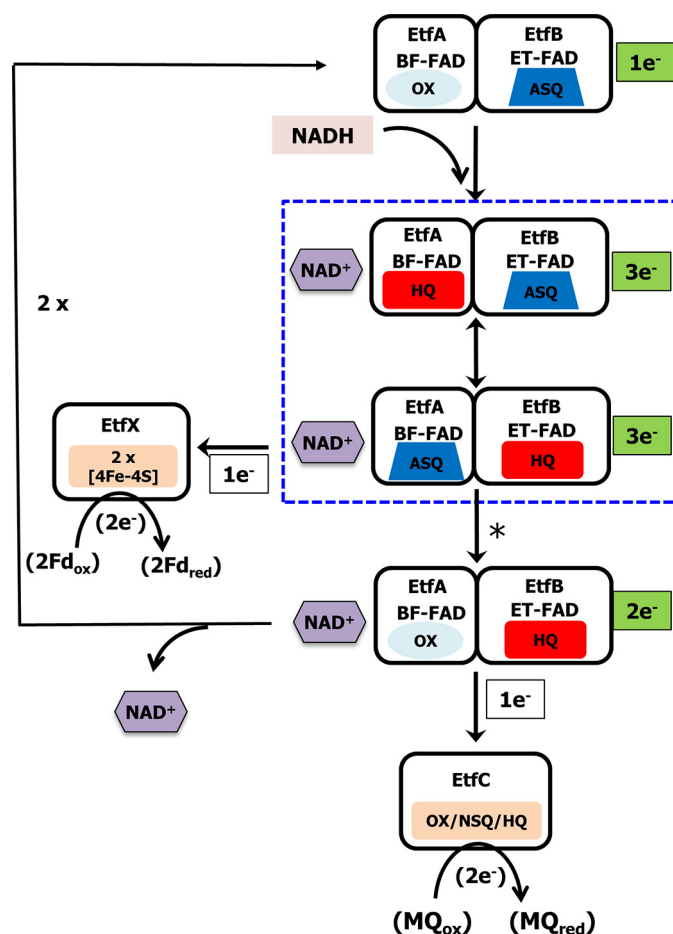
Figure 6. Proposed catalytic cycle of EtfABCX. The complex is depicted in its bifurcation-ready state in which the ET-FAD is in the ASQ state. In the first round of NADH oxidation, the BF-FAD is reduced to the HQ state and forms a CT complex with NAD⁺. The first electron is transferred to the ASQ-ET-FAD to generate the HQ state, leaving the ASQ-BF-FAD. The transfer of an electron to the low-potential branch [4Fe-4S] cluster triggers a protein conformational change (indicated by the *asterisk*) that then enables HQ-ET-FAD to reduce the FAD of EtfC with 1 e⁻ converting it to the NSQ state. The catalytic cycle continues with the oxidation of a second NADH and the transfer of electrons down the low- and high-potential branches leading to the reduction of Fd and MQ, respectively. *Boxed* with a *blue dotted line* are the complexes with NAD⁺ that could form CT complexes.

tron on HQ-ET-FAD cannot reduce the highly crossed BF-FAD, so it can only be transferred to EtfC, thereby returning the EtfAB core to its bifurcation-ready 1 e⁻ reduced state (Fig. 6). It is not clear when NAD⁺ leaves the EtfAB core, but we assume that it is after or in conjunction with transfer of the low-potential electron from the BF-FAD.

Once the 1 e⁻ reduced EtfAB core of EtfABCX is generated by loss of the high-potential electron, the enzyme then undergoes a second round of reduction by NADH. Note that only the first round of NADH oxidation is shown in Fig. 6. Hence, to complete the overall 4 e⁻ reaction (Reaction 1), a second NADH binds, a second molecule of Fd is reduced via EtfX, and a second electron is transferred to NSQ-QR-FAD, which in its fully reduced HQ form reduces one molecule of MQ. Thus, the two rounds of bifurcation that constitute the catalytic cycle of EtfABCX (Reaction 1) are in essence the same in terms of the BF- and ET-FAD, where the second NADH interacts with the

same bifurcation-ready 1 e⁻ reduced form of the EtfAB sub-complex as the first NADH.

It is important to point out that our proposed mechanism (Fig. 6) eliminates the possibility of the second electron from BF-FAD passing to the ET-FAD, despite the favorable thermodynamics, because the ET-FAD is fully reduced to its HQ state upon accepting the first electron derived from NADH and therefore is unable to accept a second electron (30). Thus, the strongly reducing electron of the ASQ-BF-FAD would be constrained to use the low-potential branch formed by the [4Fe-4S] clusters in EtfX. In contrast, our *in vitro* reductions of fully oxidized EtfAB enable NADH to provide two electrons and reduce the ET-FAD from the OX to the HQ state, whereupon electron transfer between HQ-ET-FAD-EtfAB and OX-ET-FAD-EtfAB generates two ASQ-ET-FAD-EtfABs, thereby explaining the formation of the ASQ state during NADH titrations (Fig. 4*A* and Fig. S9). This was also proposed for the related EtfAB–Bcd complex (16). This ASQ state is also formed in the *P. aerophilum* EtfABCX complex when all partners are present (Fig. 4*B* and Fig. S12).

Reduction of *P. aerophilum* EtfAB and EtfABCX by NADH generates a striking CT band spanning 600 to 1000 nm (Fig. 4, *A* and *B*) with little absorbance remaining at 454 nm. Chemical reduction of EtfAB and EtfABCX both generate a flavin ASQ that does not undergo further reduction with excess reductant (Figs. S6 and S11), and upon NAD⁺ binding, the optical ASQ signal disappears and a CT signal appears instead (Fig. 4*C* and Fig. S11). Previous reports on related ETF systems from mesophilic organisms either do not collect data for the full 600–1000-nm region or report much weaker absorption (16, 21). We propose that the much stronger signal seen from the *P. aerophilum* proteins is a consequence of the hyperthermophilic organism that we have used as the gene donor to produce EtfABCX. The optical spectra were collected at room temperature, which is 80 °C lower than the optimum growth temperature of *P. aerophilum* (25). In contrast, the related Etf systems caffeyl-CoA reductase (CarCDE), butyryl-CoA dehydrogenase-Etf, and FixABCX derive from mesophilic microorganisms (4, 19, 24). The enhanced stability of hyperthermophilic enzyme might intensify the effect of NAD(H) binding, leading to more distinct spectral features for the CT complexes.

With *P. aerophilum* EtfABCX, we experimentally distinguished two different CT optical signatures. Both have a broad CT feature with a maximum around 780 nm, but if NADH is used as the reductant, a second feature is seen near 680 nm (Fig. 4 (*A* and *B*) and Figs. S9 and S12). From our data, the CT complex is formed by NAD⁺ binding to the BF-FAD, and a flavin radical is present. We propose that both BF-FAD and ET-FAD are electronically coupled and influence the nature of the NAD⁺-bound complex. It was previously suggested for a related EtfAB complex that a tyrosine residue situated between the BF-FAD and ET-FAD mediates an electronic coupling between the two flavin cofactors (27). In *P. aerophilum* EtfAB, a tryptophan residue occupies this position and would also be competent to mediate such a coupling. Although a charge transfer between NADH and the OX-BF-FAD could also be possible (50, 51), this is inconsistent with both the radical EPR signal and the absence of an optical

signature expected from the ET-FAD ASQ. The exact nature of the NAD⁺-bound complexes in *P. aerophilum* EtfABCX is therefore unclear at present.

The reaction mechanism of *P. aerophilum* EtfABCX involves a bifurcating flavin with crossed potentials, where removing one electron from the HQ state generates a high-energy intermediate (ASQ) with a potential lower than that of the donor electron pair (from NADH) that is capable of ultimately reducing Fd (1, 31), although it should be noted that crossed potentials may not be an absolute requirement for bifurcating activity (52). It is generally accepted that this ASQ derived from a highly crossed BF-FAD is "unstable" (53). In our new NAD⁺-dependent mechanism, we propose that the formation of a NAD⁺ BF-FAD complex might protect this high-energy low-potential site from potentially harmful chemical reactions, especially when the EtfAB core is not complexed with its partners (Fig. 6). For example, it was previously shown that molecular oxygen can be reduced by the analogous EtfAB–Bcd complex, and this leads to formation of superoxide with potentially disastrous consequences for the cell (22). Based on our reaction scheme (Fig. 6), we propose that the addition of NADH to the EtfAB–Bcd complex also forms a NAD⁺ BF-FAD complex and that, in the absence of the high-potential substrate (crotonyl-CoA), this minimizes reaction of the BF-FAD with oxygen. Protection of a flavin site from oxygen through formation of a NAD⁺ complex to prevent the formation of damaging superoxide has been shown before with enzymes such as toluene dioxygenase and NADH quinone oxidoreductase (54, 55). The formation of a NAD⁺ charge transfer complex might therefore be an integral feature of EtfAB complexes and play an important role not only in its mechanism but also in protecting the cell from reactive oxygen species, a particularly important feature in (micro)aerophilic microorganisms, such as *P. aerophilum* (8, 29, 30, 48). Unexpectedly, we did not observe the complete 4 e⁻ reduced form of EtfAB (or the EtfABCX equivalent) with either the physiological electron donor NADH or with an artificial reductant. This interesting characteristic of the EtfAB core is presumably related to the formation of the NAD⁺ BF-FAD complex, although the reason for this and the detailed nature of the different electronic states will be a topic of future studies.

The only other type of bifurcating enzyme that has been studied in detail mechanistically is the phylogenetically unrelated NfnI of *P. furiosus* (31). At first glance, this catalyzes a similar reaction to that of *P. aerophilum* EtfABCX, except that the high-potential acceptor is NAD rather than quinone (Fig. 1). However, other than a common site (BF-FAD) to bifurcate the two electrons from the hydride transfer from NAD(P)H, the proposed catalytic cycle of *P. aerophilum* EtfABCX (Fig. 6) is very different from that of NfnI (Fig. S13). In both enzymes, reduction of BF-FAD by NAD(P)H provides electrons for the high- and low-potential pathways, but the stable nicotinamide-dependent CT complex observed with EtfABCX is not evident with NfnI. In further contrast, the 1 e⁻ reduced form of EtfABCX with the ASQ state of the ET-FAD is the proposed physiological resting form, which is ready to accept a hydride from NADH to form 3 e⁻ reduced intermediates. However, the resting state

of NfnI is fully oxidized, and its reduction by NADPH generates a stable 2 e$^-$ reduced state (Fig. S13). Moreover, in Nfn, the subsequent oxidation of ASQ-BF-FAD by reduction of ET-FAD is gated by an intervening [2Fe-2S] cluster, which mediates electron flow via the ET-FAD to the high-potential acceptor (in this case, NAD$^+$) in the absence of any significant conformational change (56). In further contrast, electron flow to the high-potential pathway in EtfABCX is gated by a flavin 1 e$^-$ acceptor and a rather dramatic conformational change that enables oxidation of ET-FAD (31).

The results presented herein therefore show that, despite a common bifurcating flavin, *P. aerophilum* EtfABCX and *P. furiosus* NfnI differ by formation of a stable nicotinamide-dependent CT complex in the former and not the latter, in the nature of the resting and bifurcating-ready states of the enzymes, in how electron flow down the exergonic path is gated, and in the two 2 e$^-$ catalytic cycles that constitute the overall 4 e$^-$ bifurcation reaction. They also differ in the overall energetics of their reactions. Whereas both reduce Fd ($E_m \sim -500$ mV), the driving force for EtfABCX ($\Delta E = 250$ mV) is derived from NADH oxidation ($E^{0\prime} = -320$ mV) coupled to MQ reduction ($E^{0\prime} = -70$ mV). This provides more than twice the driving force for bifurcation than in NfnI ($\Delta E = 100$ mV), which couples the oxidation of NADPH ($E_m \sim -380$ mV, under physiological conditions) to the reduction of NAD$^+$ ($E_m \sim -280$ mV). It is not clear whether the overall energetics are related to any differences in the overall catalytic cycles for the two enzymes. This emphasizes that there might not be a general flavin-based bifurcating mechanism; rather, each type of enzyme harbors a unique reaction scheme (3, 8, 11, 12). Nevertheless, the reaction scheme shown in Fig. 6 is proposed as a framework to guide future work in elucidating more mechanistic details of the bifurcating reaction of *P. aerophilum* EtfABCX and of bifurcating ETFs in general.

Experimental procedures

Expression and purification of P. aerophilum EtfABCX

The plasmid encoding *P. aerophilum* EtfABCX was constructed with the following fragments via Gibson assembly (New England Biolabs): an 8.8-kb backbone BAC vector containing the *pyr*F genetic marker, the flanking homologous recombination region targeting the interspace between convergent genes PF1232 and PF1233, the *slp* promoter region (PF1399), and the 5.04-kb EtfBAXC genes PAE0721–0723, with a His$_9$-Ala tag at the N terminus of the EtfA subunit (PAE0725). The order of genes in this cluster was rearranged to EtfABCX (PAE0722, PAE0721, PAE0725, and PAE0723) with a *P. furious* ribosomal binding site inserted in front of each Etf subunit. This plasmid, termed pGL098, was sequence-verified and linearized before transformation of *P. furiosus* COM1 strain as described previously (57). Positive transformants were cultured and purified twice on liquid and solid defined cellobiose medium. The genomic DNA was isolated using the ZymoBead^{TM} genomic DNA kit (Zymo Research), and PCR was used for isolate screening, using a primer pair that targeted outside the homologous flanking region mentioned above. The

strain containing the EtfABCX overexpression construct was designated as MW393. All primers used in plasmid and strain construction are listed in Table S2.

Large-scale fermentation of recombinant *P. furiosus* was performed as described previously (58). Frozen cells ($\sim$100 g wet weight) were lysed in 50 mM phosphate buffer, pH 7.5, with 1 mM DTT under strict anaerobic conditions. Cell debris and membranes were removed by centrifugation at 100,000 $\times$ g. The supernatant was loaded on a 5-ml Histrap column (GE Healthcare) using the recommended phosphate buffer with the addition of 1 mM DTT. The green-colored EtfABCX started eluting when $\sim$50 mM imidazole was applied. Based on the chromatogram, the green/yellow fractions were pooled and concentrated to $\sim$5–10 ml using ultrafiltration under anaerobic conditions. The concentrated sample was applied to a Superdex S200 column (60/600; GE Healthcare) and eluted with 25 mM Tris-HCl, pH 8, containing 300 mM NaCl (but lacking DTT). Fractions corresponding to EtfAB and EtfABCX were selected on the basis of flavin content and gel electrophoresis (Miniprotean TGX stainfree gels; Bio-Rad).

Enzyme assays

NADH-linked activities of EtfAB and ABCX were measured anaerobically at 80 °C in 3-ml glass cuvettes sealed with rubber stoppers containing 50 mM HEPES, pH 7.5, 100 mM NaCl, 1 mM NADH, and 200 μM iodonitrotetrazolium chloride. The formation of the red formazan was followed at 500 nm (ϵ = 19.3 mM^{-1} cm^{-1}) in a Cary 100 UV-visible spectrophotometer with a Peltier-based temperature controller (Agilent). When menadione (100 μM) was used as electron acceptor, the activity was followed by the oxidation of NADH (200 μM, ϵ = 6.2 mM^{-1} cm^{-1} at 340 nm). Bifurcating assays were performed anaerobically in quartz 4-ml fluorescence cuvettes sealed with silicon stoppers using a RF-5301-PC fluorimeter (Shimadzu). *P. furiosus* Fd (50 μM) and menadione (100 μM) were reduced with 400 μM titanium citrate (reduction of Fd was monitored by its UV-visible spectrum). NAD$^+$ (1 mM) was added as electron acceptor, and the formation of NADH was followed by fluorescence (excitation 340 nm/emission 460 nm).

Redox titrations

Titrations were performed at 25 °C in an upcycled Agilent HP 8453 operating under OlisWorks (Olis) using 600-μl masked quartz cuvettes (Starna) anaerobically sealed with silicon stoppers. Reductant was anaerobically added in small quantities with a 10-μl gas-tight syringe (Hamilton) to samples prepared in 50 mM MOPS, pH 7.5, with 200 mM NaCl. UV-visible spectra, 200–1000 nm, were recorded after each addition. All solutions were prepared under strict anaerobic conditions, and stock solutions of titanium citrate were prepared as described previously (59).

To determine reduction midpoint potentials at pH 7.0 ($E^{0\prime}$), protein samples were prepared in 25 mM Bistris propane, pH 7.0, containing 200 mM NaCl. $E^{0\prime}$ values were measured using the xanthine/xanthine oxidase system (27, 60, 61). Attainment of equilibrium was confirmed by comparing $E^{0\prime}$ values obtained

in slower and faster titrations; 40 min was typical (62), and all titrations were performed in duplicate or more. The dyes used were thionin acetate ($n_{Dye} = 2$, $E^{0'}_{Dye} = +56$ mV, $\lambda_{max} = 598$ nm), Nile blue chloride ($n_{Dye} = 2$, $E^{0'}_{Dye} = -116$ mV, $\lambda_{max} = 636$ nm), and safranin-O ($n_{Dye} = 2$, $E^{0'}_{Dye} = -289$ mV, $\lambda_{max} = 520$ nm, and the dye isosbestic at 412 nm was used for monitoring the flavin). Data were analyzed using Equation 1 derived by equating the Nernst equation for the dye with that of the enzyme, at equilibrium with the dye, for the example of the OX/ASQ couple. At each point in the titrations,

$$\log_{10}\frac{[Ox_{FAD}]}{[Red_{FAD}]} = \frac{n_{FAD}}{n_{Dye}}\log_{10}\frac{[Ox_{Dye}]}{[Red_{Dye}]} + \frac{n_{FAD}F}{RT\ln 10}(E^0_{Dye} - E^0_{FAD/FAD^{\bar{}}})$$

(Eq. 1)

the concentrations of oxidized and reduced dye and reacting flavin were determined from the absorbance values of each at the appropriate wavelength. To focus on only the one flavin undergoing reduction in each phase of reduction, difference spectra were used. In these, the final spectrum of each phase was subtracted from each other spectrum in the phase, and the three phases were identified by noting the different changes in A_{374} characterizing initial reduction of OX to ASQ, ASQ to HQ, and OX to HQ (Fig. S6). Thus, we calculated the concentration of FAD or dye remaining in the oxidized state of the reaction under consideration ($[Ox_{FAD}]$ or $[Ox_{dye}]$), and from these and the total concentrations, we obtained the concentrations of the corresponding reduced states ($[Red_{FAD}]$ or $[Red_{dye}]$). Plots of $\log_{10}([Ox_{FAD}]/[Red_{FAD}^{\bar{}}])$ *versus* $\log_{10}([Ox_{Dye}]/[Red_{Dye}])$ then yielded n_{FAD}, the number of electrons taken up by the FAD revealing the nature of each reaction, from the magnitude of the slope, $m = n_{FAD}/n_{dye}$. The intercept with the vertical axis at $\log([Ox_{dye}]/[Red_{dye}]) = 0$, b, then yielded the flavin $E^{0'}$ of the reaction from $b = n_{FAD}(E^{0'}_{Dye} - E^{0'}_{FAD})/25.7$ mV, where 25.7 mV replaces the physical constants and temperature RT/F ($T = 25$ °C), and all $E^{0'}$ values are quoted *versus* the normal hydrogen electrode.

EPR spectroscopy

Samples of *P. aerophilum* EtfAB and EtfABCX were prepared for analysis by EPR spectroscopy under strictly anaerobic conditions in an N_2 atmosphere glove box (MBraun). Both EtfAB (150 μM) and EtfABCX (120 μM) were prepared in 25 mM Tris buffer containing 300 mM NaCl and 5% (v/v) glycerol. EtfAB was treated with either NADH (1 mM), sodium dithionite (10 mM), or sequential treatments of sodium dithionite (10 mM) and NAD^+ (10 mM). For the latter, NAD^+ was added to a thawed sample that had been initially treated and frozen with sodium dithionite. All samples were prepared in sealed tubes and slowly frozen in liquid N_2. EPR spectra were recorded with a Bruker E-500 spectrometer (X-band, 9.38 GHz) equipped with an SHQ resonator, an in-cavity cryogen-free VT system (ColdEdge Technologies), and a MercuryiTC temperature controller (Oxford). EPR parameters for measuring radical signals were as follows: modulation frequency, 100 kHz; modulation amplitude, 2 G; microwave power, 1 milliwatt; temperature, 77 K. EPR parameters for measuring [Fe-S] signals were as follows: modulation frequency, 100 kHz; modulation amplitude, 10 G;

microwave power, 1 milliwatt; temperature, 10 K. Spin quantification of radical signals was carried out by comparison of signal intensities with standards using HO-TEMPO (4-hydroxy-2,2,6,6-tetramethylpiperidine 1-oxy, 5–100 μM concentration) and double integration of the spectra using the OriginPro software package.

TAS

The ultrafast (100 fs to 5.1 ns) TAS spectrometer employed here was operated as described previously (31). The pump wavelength was 400 nm for sample excitation, and the experiment was conducted at room temperature. For all measurements, the sample was prepared in an Mbraun glove box (N_2 atmosphere), sealed in a 2-mm quartz cuvette, and constantly stirred to prevent photodegradation. The concentrations of *P. aerophilum* EtfAB and EtfABCX were ~150 and 100 μM, respectively. The data collection (350 pump shots per time point) was carried out four consecutive times and then averaged. The experiment was repeated two times. Data were corrected for spectral chirp using SurfaceXplorer (Ultrafast Systems). Fitting was performed in Igor Pro using single- or double-exponential fit functions.

MS analysis

Protein identification (63), intact protein analysis (64), and protein–protein interaction analysis (24, 65) were performed as described previously. The *P. aerophilum* EtfABCX complex (7.9 μM) was surface-labeled with 0.3 mM DnsCl (Acros) in a 100 mM sodium phosphate buffer, pH 8.0, at 25 °C. The reaction was quenched after 5, 15, and 30 min with 2 μl of 100 mM ammonium acetate, pH 8.0. Samples were digested with trypsin followed by LC-MS/MS analysis (63). Native MS experiments were conducted on a SYNAPT G2-*Si* instrument (Waters) (66). Samples were exchanged to 500 mM ammonium acetate, pH 7.0 (Sigma), and infused from in-house prepared gold-coated borosilicate glass capillaries at a protein concentration of 1.5 μM and a flow rate of 90 nl min^{-1}. Data analysis was performed in MassLynx version 4.1 (Waters). The EtfABCX model was produced using Swiss Modeler (67), followed by manual adjustment of a few side chains and unstructured strands and then energy minimization in Chimera (68). These were tested on the basis of the fit of the cofactors from the template structures within the modeled *P. aerophilum* components.

References

1. Peters, J. W., Miller, A. F., Jones, A. K., King, P. W., and Adams, M. W. (2016) Electron bifurcation. *Curr. Opin. Chem. Biol.* **31,** 146–152 CrossRef Medline

2. Brandt, U. (1996) Bifurcated ubihydroquinone oxidation in the cytochrome bc1 complex by proton-gated charge transfer. *FEBS Lett.* **387,** 1–6 CrossRef Medline

3. Buckel, W., and Thauer, R. K. (2013) Energy conservation via electron bifurcating ferredoxin reduction and proton/Na$^+$ translocating ferredoxin oxidation. *Biochim. Biophys. Acta* **1827,** 94–113 CrossRef Medline

4. Li, F., Hinderberger, J., Seedorf, H., Zhang, J., Buckel, W., and Thauer, R. K. (2008) Coupled ferredoxin and crotonyl coenzyme A (CoA) reduction with NADH catalyzed by the butyryl-CoA dehydrogenase/Etf complex from *Clostridium kluyveri. J. Bacteriol.* **190,** 843–850 CrossRef Medline

5. Metcalf, W. W. (2016) Classic spotlight: electron bifurcation, a unifying concept for energy conservation in anaerobes. *J. Bacteriol.* **198,** 1358 CrossRef Medline

6. Mitchell, P. (1976) Possible molecular mechanisms of the protonmotive function of cytochrome systems. *J. Theor. Biol.* **62,** 327–367 CrossRef Medline

7. Schut, G. J., and Adams, M. W. (2009) The iron-hydrogenase of *Thermotoga maritima* utilizes ferredoxin and NADH synergistically: a new perspective on anaerobic hydrogen production. *J. Bacteriol.* **191,** 4451–4457 CrossRef Medline

8. Buckel, W., and Thauer, R. K. (2018) Flavin-based electron bifurcation, a new mechanism of biological energy coupling. *Chem. Rev.* **118,** 3862–3886 CrossRef Medline

9. Herrmann, G., Jayamani, E., Mai, G., and Buckel, W. (2008) Energy conservation via electron-transferring flavoprotein in anaerobic bacteria. *J. Bacteriol.* **190,** 784–791 CrossRef Medline

10. Buckel, W., and Thauer, R. K. (2018) Flavin-based electron bifurcation, ferredoxin, flavodoxin, and anaerobic respiration with protons (Ech) or NAD$^+$ (Rnf) as electron acceptors: a historical review. *Front. Microbiol.* **9,** 401 CrossRef Medline

11. Peters, J. W., Beratan, D. N., Schut, G. J., and Adams, M. W. W. (2018) On the nature of organic and inorganic centers that bifurcate electrons, coupling exergonic and endergonic oxidation-reduction reactions. *Chem. Commun.* **54,** 4091–4099 CrossRef Medline

12. Peters, J. W., Beratan, D. N., Bothner, B., Dyer, R. B., Harwood, C. S., Heiden, Z. M., Hille, R., Jones, A. K., King, P. W., Lu, Y., Lubner, C. E., Minteer, S. D., Mulder, D. W., Raugei, S., Schut, G. J., *et al.* (2018) A new era for electron bifurcation. *Curr. Opin. Chem. Biol.* **47,** 32–38 CrossRef Medline

13. Garcia Costas, A. M., Poudel, S., Miller, A. F., Schut, G. J., Ledbetter, R. N., Fixen, K. R., Seefeldt, L. C., Adams, M. W. W., Harwood, C. S., Boyd, E. S., and Peters, J. W. (2017) Defining electron bifurcation in the electron-transferring flavoprotein family. *J. Bacteriol.* **199,** e00440-e00417 Medline

14. Toogood, H. S., Leys, D., and Scrutton, N. S. (2007) Dynamics driving function: new insights from electron transferring flavoproteins and partner complexes. *FEBS J.* **274,** 5481–5504 CrossRef Medline

15. Tsai, M. H., and Saier, M. H., Jr. (1995) Phylogenetic characterization of the ubiquitous electron transfer flavoprotein families ETF-α and ETF-β. *Res. Microbiol.* **146,** 397–404 CrossRef Medline

16. Chowdhury, N. P., Mowafy, A. M., Demmer, J. K., Upadhyay, V., Koelzer, S., Jayamani, E., Kahnt, J., Hornung, M., Demmer, U., Ermler, U., and Buckel, W. (2014) Studies of the mechanism of electron bifurcation catalyzed by electron transferring flavoprotein (Etf) and butyryl-CoA dehydrogenase (Bcd) of *Acidaminococcus fermentans. J. Biol. Chem.* **289,** 5145–5157 CrossRef Medline

17. Sato, K., Nishina, Y., and Shiga, K. (2003) Purification of electron-transferring flavoprotein from *Megasphaera elsdenii* and binding of additional FAD with an unusual absorption spectrum. *J. Biochem.* **134,** 719–729 CrossRef Medline

18. Weghoff, M. C., Bertsch, J., and Müller, V. (2015) A novel mode of lactate metabolism in strictly anaerobic bacteria. *Environ. Microbiol.* **17,** 670–677 CrossRef Medline

19. Bertsch, J., Parthasarathy, A., Buckel, W., and Müller, V. (2013) An electron-bifurcating caffeyl-CoA reductase. *J. Biol. Chem.* **288,** 11304–11311 CrossRef Medline

20. Brockman, H. L., and Wood, W. A. (1975) D-Lactate dehydrogenase of *Peptostreptococcus elsdenii. J. Bacteriol.* **124,** 1454–1461 Medline

21. Sato, K., Nishina, Y., and Shiga, K. (2013) Interaction between NADH and electron-transferring flavoprotein from *Megasphaera elsdenii. J. Biochem.* **153,** 565–572 CrossRef Medline

22. Chowdhury, N. P., Kahnt, J., and Buckel, W. (2015) Reduction of ferredoxin or oxygen by flavin-based electron bifurcation in *Megasphaera elsdenii. FEBS J.* **282,** 3149–3160 CrossRef Medline

23. Edgren, T., and Nordlund, S. (2004) The *fixABCX* genes in *Rhodospirillum rubrum* encode a putative membrane complex participating in electron transfer to nitrogenase. *J. Bacteriol.* **186,** 2052–2060 CrossRef Medline

24. Ledbetter, R. N., Garcia Costas, A. M., Lubner, C. E., Mulder, D. W., Tokmina-Lukaszewska, M., Artz, J. H., Patterson, A., Magnuson, T. S., Jay, Z. J., Duan, H. D., Miller, J., Plunkett, M. H., Hoben, J. P., Barney, B. M., Carlson, R. P., *et al.* (2017) The electron bifurcating FixABCX protein complex from *Azotobacter vinelandii*: generation of low-potential reducing equivalents for nitrogenase catalysis. *Biochemistry* **56,** 4177–4190 CrossRef Medline

25. Völkl, P., Huber, R., Drobner, E., Rachel, R., Burggraf, S., Trincone, A., and Stetter, K. O. (1993) *Pyrobaculum aerophilum* sp. nov., a novel nitrate-reducing hyperthermophilic archaeum. *Appl. Environ. Microbiol.* **59,** 2918–2926 Medline

26. Fitz-Gibbon, S. T., Ladner, H., Kim, U. J., Stetter, K. O., Simon, M. I., and Miller, J. H. (2002) Genome sequence of the hyperthermophilic crenarchaeon *Pyrobaculum aerophilum. Proc. Natl. Acad. Sci. U.S.A.* **99,** 984–989 CrossRef Medline

27. Duan, H. D., Lubner, C. E., Tokmina-Lukaszewska, M., Gauss, G. H., Bothner, B., King, P. W., Peters, J. W., and Miller, A. F. (2018) Distinct properties underlie flavin-based electron bifurcation in a novel electron transfer flavoprotein FixAB from *Rhodopseudomonas palustris. J. Biol. Chem.* **293,** 4688–4701 CrossRef Medline

28. Watmough, N. J., and Frerman, F. E. (2010) The electron transfer flavoprotein: ubiquinone oxidoreductases. *Biochim. Biophys. Acta* **1797,** 1910–1916 CrossRef Medline

29. Demmer, J. K., Bertsch, J., Öppinger, C., Wohlers, H., Kayastha, K., Demmer, U., Ermler, U., and Müller, V. (2018) Molecular basis of the flavin-based electron-bifurcating caffeyl-CoA reductase reaction. *FEBS Lett.* **592,** 332–342 CrossRef Medline

30. Demmer, J. K., Pal Chowdhury, N., Selmer, T., Ermler, U., and Buckel, W. (2017) The semiquinone swing in the bifurcating electron transferring flavoprotein/butyryl-CoA dehydrogenase complex from *Clostridium difficile. Nat. Commun.* **8,** 1577 CrossRef Medline

31. Lubner, C. E., Jennings, D. P., Mulder, D. W., Schut, G. J., Zadvornyy, O. A., Hoben, J. P., Tokmina-Lukaszewska, M., Berry, L., Nguyen, D. M., Lipscomb, G. L., Bothner, B., Jones, A. K., Miller, A. F., King, P. W., Adams, M. W. W., and Peters, J. W. (2017) Mechanistic insights into energy conservation by flavin-based electron bifurcation. *Nat. Chem. Biol.* **13,** 655–659 CrossRef Medline

32. Kelley, L. A., Mezulis, S., Yates, C. M., Wass, M. N., and Sternberg, M. J. (2015) The Phyre2 web portal for protein modeling, prediction and analysis. *Nat. Protoc.* **10,** 845–858 CrossRef Medline

33. Song, Y., Nelp, M. T., Bandarian, V., and Wysocki, V. H. (2015) Refining the structural model of a heterohexameric protein complex: surface induced dissociation and ion mobility provide key connectivity and topology information. *ACS Cent. Sci.* **1,** 477–487 CrossRef Medline

34. Baud, A., Gonnet, F., Salard, I., Le Mignon, M., Giuliani, A., Mercère, P., Sclavi, B., and Daniel, R. (2016) Probing the solution structure of Factor H using hydroxyl radical protein footprinting and cross-linking. *Biochem. J.* **473,** 1805–1819 CrossRef Medline

35. Fernandez-Martinez, J., Kim, S. J., Shi, Y., Upla, P., Pellarin, R., Gagnon, M., Chemmama, I. E., Wang, J., Nudelman, I., Zhang, W., Williams, R., Rice, W. J., Stokes, D. L., Zenklusen, D., Chait, B. T., Sali, A., and Rout, M. P. (2016) Structure and function of the nuclear pore complex cytoplasmic mRNA export platform. *Cell* **167,** 1215–1228.e25 CrossRef Medline

36. Liu, W. H., Roemer, S. C., Zhou, Y., Shen, Z. J., Dennehey, B. K., Balsbaugh, J. L., Liddle, J. C., Nemkov, T., Ahn, N. G., Hansen, K. C., Tyler, J. K., and Churchill, M. E. (2016) The Cac1 subunit of histone chaperone CAF-1 organizes CAF-1-H3/H4 architecture and tetramerizes histones. *Elife* **5,** e18023 CrossRef Medline

37. Mummadisetti, M. P., Frankel, L. K., Bellamy, H. D., Sallans, L., Goettert, J. S., Brylinski, M., Limbach, P. A., and Bricker, T. M. (2014) Use of protein cross-linking and radiolytic footprinting to elucidate PsbP and PsbQ interactions within higher plant Photosystem II. *Proc. Natl. Acad. Sci. U.S.A.* **111,** 16178–16183 CrossRef Medline

38. Schmidt, C., Zhou, M., Marriott, H., Morgner, N., Politis, A., and Robinson, C. V. (2013) Comparative cross-linking and mass spectrometry of an intact F-type ATPase suggest a role for phosphorylation. *Nat. Commun.* **4,** 1985 CrossRef Medline

39. Zanphorlin, L. M., Lima, T. B., Wong, M. J., Balbuena, T. S., Minetti, C. A., Remeta, D. P., Young, J. C., Barbosa, L. R., Gozzo, F. C., and Ramos, C. H. (2016) Heat shock protein 90 kDa (Hsp90) has a second functional interaction site with the mitochondrial import receptor Tom70. *J. Biol. Chem.* **291,** 18620–18631 CrossRef Medline

40. Merkley, E. D., Rysavy, S., Kahraman, A., Hafen, R. P., Daggett, V., and Adkins, J. N. (2014) Distance restraints from crosslinking mass spectrometry: mining a molecular dynamics simulation database to evaluate lysine-lysine distances. *Protein Sci.* **23,** 747–759 CrossRef Medline

41. Hagedoorn, P. L., Chen, T., Schröder, I., Piersma, S. R., de Vries, S., and Hagen, W. R. (2005) Purification and characterization of the tungsten enzyme aldehyde:ferredoxin oxidoreductase from the hyperthermophilic denitrifier *Pyrobaculum aerophilum. J. Biol. Inorg. Chem.* **10,** 259–269 CrossRef Medline

42. Elling, F. J., Becker, K. W., Könneke, M., Schröder, J. M., Kellermann, M. Y., Thomm, M., and Hinrichs, K. U. (2016) Respiratory quinones in Archaea: phylogenetic distribution and application as biomarkers in the marine environment. *Environ. Microbiol.* **18,** 692–707 CrossRef Medline

43. Nguyen, D. M. N., Schut, G. J., Zadvornyy, O. A., Tokmina-Lukaszewska, M., Poudel, S., Lipscomb, G. L., Adams, L. A., Dinsmore, J. T., Nixon, W. J., Boyd, E. S., Bothner, B., Peters, J. W., and Adams, M. W. W. (2017) Two functionally distinct NADP$^+$-dependent ferredoxin oxidoreductases maintain the primary redox balance of *Pyrococcus furiosus. J. Biol. Chem.* **292,** 14603–14616 CrossRef Medline

44. Iyanagi, T. (1977) Redox properties of microsomal reduced nicotinamide adenine dinucleotide-cytochrome b_5 reductase and cytochrome b_5. *Biochemistry* **16,** 2725–2730 CrossRef Medline

45. Medina, M., Gomez-Moreno, C., and Cammack, R. (1995) Electron spin resonance and electron nuclear double resonance studies of flavoproteins involved in the photosynthetic electron transport in the cyanobacterium *Anabaena* sp. PCC 7119. *Eur. J. Biochem.* **227,** 529–536 CrossRef Medline

46. DeRose, V. J., Woo, J. C., Hawe, W. P., Hoffman, B. M., Silverman, R. B., and Yelekci, K. (1996) Observation of a flavin semiquinone in the resting state of monoamine oxidase B by electron paramagnetic resonance and electron nuclear double resonance spectroscopy. *Biochemistry* **35,** 11085–11091 CrossRef Medline

47. Deistung, J., and Thorneley, R. N. F. (1986) Electron transfer to nitrogenase. Characterization of flavodoxin from *Azotobacter chroococcum* and comparison of its redox potentials with those of flavodoxins from *Azotobacter vinelandii* and *Klebsiella pneumoniae* (*nifF*-gene product). *Biochem. J.* **239,** 69–75 CrossRef Medline

48. Bergdoll, L., Ten Brink, F., Nitschke, W., Picot, D., and Baymann, F. (2016) From low- to high-potential bioenergetic chains: thermodynamic con-

straints of Q-cycle function. *Biochim. Biophys. Acta* **1857,** 1569–1579 CrossRef Medline

49. Page, C. C., Moser, C. C., Chen, X., and Dutton, P. L. (1999) Natural engineering principles of electron tunnelling in biological oxidation-reduction. *Nature* **402,** 47–52 CrossRef Medline

50. Peregrina, J. R., Sánchez-Azqueta, A., Herguedas, B., Martínez-Júlvez, M., and Medina, M. (2010) Role of specific residues in coenzyme binding, charge-transfer complex formation, and catalysis in *Anabaena* ferredoxin NADP$^+$-reductase. *Biochim. Biophys. Acta* **1797,** 1638–1646 CrossRef Medline

51. Batie, C. J., and Kamin, H. (1986) Association of ferredoxin-NADP$^+$ reductase with NADP(H) specificity and oxidation-reduction properties. *J. Biol. Chem.* **261,** 11214–11223 Medline

52. Zhang, P., Yuly, J. L., Lubner, C. E., Mulder, D. W., King, P. W., Peters, J. W., and Beratan, D. N. (2017) Electron bifurcation: thermodynamics and kinetics of two-electron brokering in biological redox chemistry. *Acc. Chem. Res.* **50,** 2410–2417 CrossRef Medline

53. Nitschke, W., and Russell, M. J. (2012) Redox bifurcations: mechanisms and importance to life now, and at its origin: a widespread means of energy conversion in biology unfolds. *Bioessays* **34,** 106–109 CrossRef Medline

54. Lin, T. Y., Werther, T., Jeoung, J. H., and Dobbek, H. (2012) Suppression of electron transfer to dioxygen by charge transfer and electron transfer complexes in the FAD-dependent reductase component of toluene dioxygenase. *J. Biol. Chem.* **287,** 38338–38346 CrossRef Medline

55. Sena, F. V., Sousa, F. M., Oliveira, A. S. F., Soares, C. M., Catarino, T., and Pereira, M. M. (2018) Regulation of the mechanism of Type-II NADH: quinone oxidoreductase from *S. aureus. Redox Biol.* **16,** 209–214 CrossRef Medline

56. Berry, L., Poudel, S., Tokmina-Lukaszewska, M., Colman, D. R., Nguyen, D. M. N., Schut, G. J., Adams, M. W. W., Peters, J. W., Boyd, E. S., and Bothner, B. (2018) H/D exchange mass spectrometry and statistical coupling analysis reveal a role for allostery in a ferredoxin-dependent bifurcating transhydrogenase catalytic cycle. *Biochim. Biophys. Acta Gen. Subj.* **1862,** 9–17 CrossRef Medline

57. Lipscomb, G. L., Stirrett, K., Schut, G. J., Yang, F., Jenney, F. E., Jr, Scott, R. A., Adams, M. W., and Westpheling, J. (2011) Natural competence in the hyperthermophilic archaeon *Pyrococcus furiosus* facilitates genetic manipulation: construction of markerless deletions of genes encoding the two cytoplasmic hydrogenases. *Appl. Environ. Microbiol.* **77,** 2232–2238 CrossRef Medline

58. Verhagen, M. F., Menon, A. L., Schut, G. J., and Adams, M. W. (2001) *Pyrococcus furiosus*: large-scale cultivation and enzyme purification. *Methods Enzymol.* **330,** 25–30 CrossRef Medline

59. Zehnder, A. J., and Wuhrmann, K. (1976) Titanium (III) citrate as a nontoxic oxidation-reduction buffering system for the culture of obligate anaerobes. *Science* **194,** 1165–1166 CrossRef Medline

60. Efimov, I., Parkin, G., Millett, E. S., Glenday, J., Chan, C. K., Weedon, H., Randhawa, H., Basran, J., and Raven, E. L. (2014) A simple method for the determination of reduction potentials in heme proteins. *FEBS Lett.* **588,** 701–704 CrossRef Medline

61. Massey, V. (1991) A simple method for determination of redox potentials. in *Flavins and Flavoproteins* (Curti, B., Ronchi, S., and Zanetti, G., eds) pp. 59–66, Walter de Gruyter, Berlin

62. Trimmer, E. E., Ballou, D. P., Galloway, L. J., Scannell, S. A., Brinker, D. R., and Casas, K. R. (2005) Aspartate 120 of *Escherichia coli* methylenetetrahydrofolate reductase: evidence for major roles in folate binding and catalysis and a minor role in flavin reactivity. *Biochemistry* **44,** 6809–6822 CrossRef Medline

63. Yang, Z. Y., Ledbetter, R., Shaw, S., Pence, N., Tokmina-Lukaszewska, M., Eilers, B., Guo, Q., Pokhrel, N., Cash, V. L., Dean, D. R., Antony, E., Bothner, B., Peters, J. W., and Seefeldt, L. C. (2016) Evidence that the P$_i$ release event is the rate-limiting step in the nitrogenase catalytic cycle. *Biochemistry* **55,** 3625–3635 CrossRef Medline

64. Poudel, S., Tokmina-Lukaszewska, M., Colman, D. R., Refai, M., Schut, G. J., King, P. W., Maness, P. C., Adams, M. W., Peters, J. W., Bothner, B., and Boyd, E. S. (2016) Unification of [FeFe]-hydrogenases into three struc-

tural and functional groups. *Biochim. Biophys. Acta* **1860,** 1910–1921 CrossRef Medline

65. Zhang, H., Wen, J., Huang, R. Y., Blankenship, R. E., and Gross, M. L. (2012) Mass spectrometry-based carboxyl footprinting of proteins: method evaluation. *Int. J. Mass Spectrom.* **312,** 78–86 CrossRef Medline

66. Luo, M. L., Jackson, R. N., Denny, S. R., Tokmina-Lukaszewska, M., Maksimchuk, K. R., Lin, W., Bothner, B., Wiedenheft, B., and Beisel, C. L. (2016) The CRISPR RNA-guided surveillance complex in *Escherichia coli* accommodates extended RNA spacers. *Nucleic Acids Res.* **44,** 7385–7394 Medline

67. Biasini, M., Bienert, S., Waterhouse, A., Arnold, K., Studer, G., Schmidt, T., Kiefer, F., Gallo Cassarino, T., Bertoni, M., Bordoli, L., and Schwede, T. (2014) SWISS-MODEL: modelling protein tertiary and quaternary structure using evolutionary information. *Nucleic Acids Res.* **42,** W252–W258 CrossRef Medline

68. Pettersen, E. F., Goddard, T. D., Huang, C. C., Couch, G. S., Greenblatt, D. M., Meng, E. C., and Ferrin, T. E. (2004) UCSF Chimera–a visualization system for exploratory research and analysis. *J. Comput. Chem.* **25,** 1605–1612 CrossRef Medline

ASBMB